

Coherent singlet–triplet oscillations in a silicon-based double quantum dot

B. M. Maune¹, M. G. Borselli¹, B. Huang¹, T. D. Ladd¹, P. W. Deelman¹, K. S. Holabird¹, A. A. Kiselev¹, I. Alvarado-Rodriguez¹, R. S. Ross¹, A. E. Schmitz¹, M. Sokolich¹, C. A. Watson¹, M. F. Gyure¹ & A. T. Hunter¹

Silicon is more than the dominant material in the conventional microelectronics industry: it also has potential as a host material for emerging quantum information technologies. Standard fabrication techniques already allow the isolation of single electron spins in silicon transistor-like devices. Although this is also possible in other materials, silicon-based systems have the advantage of interacting more weakly with nuclear spins. Reducing such interactions is important for the control of spin quantum bits because nuclear fluctuations limit quantum phase coherence, as seen in recent experiments in GaAs-based quantum dots^{1,2}. Advances in reducing nuclear decoherence effects by means of complex control^{3–5} still result in coherence times much shorter than those seen in experiments on large ensembles of impurity-bound electrons in bulk silicon crystals^{6,7}. Here we report coherent control of electron spins in two coupled quantum dots in an undoped Si/SiGe heterostructure and show that this system has a nuclei-induced dephasing time of 360 nanoseconds, which is an increase by nearly two orders of magnitude over similar measurements in GaAs-based quantum dots. The degree of phase coherence observed, combined with fast, gated electrical initialization, read-out and control, should motivate future development of silicon-based quantum information processors.

Coherent control of single, isolated quantum bits (qubits) has now been demonstrated in a large variety of physical systems⁸, but not in silicon. Silicon qubits have garnered interest for over a decade in part owing to the potential to exploit techniques and infrastructure from the established microelectronics industry^{9,10}. Interest in silicon is further supported by the expectation of the material's superior spin coherence times relative to other semiconductors, a result of both the reduced hyperfine coupling to nuclear spins in the semiconducting host material and the reduced number of nuclear spins. Despite the significant interest in silicon-based electrically gated qubits, progress has been hampered by several fabrication and design challenges. For example, the larger in-plane effective electron mass in silicon (which is nearly three times larger than in GaAs) shrinks the electron wavefunctions where the quantum dots are formed. Smaller wavefunctions necessitate the fabrication of correspondingly smaller devices to facilitate the isolation of a single electron in each dot. Another concern is the valley degeneracy present in bulk silicon, which is removed by an appropriate combination of strain, spatial confinement and interface properties. Considerable progress has been made in overcoming these and other obstacles, and has led to recent measurements demonstrating sufficiently large valley splitting and sufficiently long spin relaxation times for spin-qubit initialization and read-out operations^{11–19}.

In the present work, we form quantum dots by depleting charge from a two-dimensional electron gas within a Si/SiGe undoped heterostructure with lithographically patterned electrostatic gates (Fig. 1). We adjust the carrier concentration within the silicon quantum well using an isolated global gate above the device, and we control the charge states of the two quantum dots using the other gate electrodes. After initially depleting the double dot of all but two electrons (with

one in each dot), we optimize the coupling of the quantum dots and electron-bath tunnel barriers to allow coherent dot manipulations. This and similar devices and the design advances that have facilitated coherent operation are further described in ref. 11; the work presented here used device C of that report.

As previously described¹ for a GaAs double quantum dot, the coherent electron manipulations we discuss involve operating the silicon double dot in the (1,1) charge configuration, where two electrons are separated with one in each dot. In this configuration and at a finite magnetic field, which splits off the $m = \pm 1$ spin triplet states, (1,1) T_{\pm} , the spin singlet state, (1,1) S , and the $m = 0$ spin triplet state, (1,1) T_0 , may be treated as the two states of a qubit (Supplementary Information). To measure these states, we rely on spin-to-charge conversion based on Pauli spin blockade. Figure 2a shows a spin blockade signature at the (0,2)–(1,1) anticrossing obtained by cyclically pulsing the gates to transfer the double dot through the (0,1) \rightarrow (1,1) \rightarrow (0,2) sequence. During the (0,1) \rightarrow (1,1) transition, an electron is loaded from the bath into the left-hand dot. Both singlet and triplet states, including states formed from different valleys, are populated. Whereas the lowest-energy singlet state is able to freely transfer into (0,2), other states, including the lowest-energy triplet, are blocked by the Pauli exclusion principle^{15,20–22}. This blockade is indicated by a change in the conductance of a nearby quantum point contact (QPC), which discriminates between the (1,1) and (0,2) dot charge states. The measured (0,2) signal level is used to define 100% singlet probability in subsequent experiments. The conductance change between (1,1) and (0,2), together with the known fractional time spent in the measure phase and an experimentally estimated amount of blockade relaxation during measurement, allows us directly to convert measured signal to singlet probability for all data presented here (Supplementary Information).

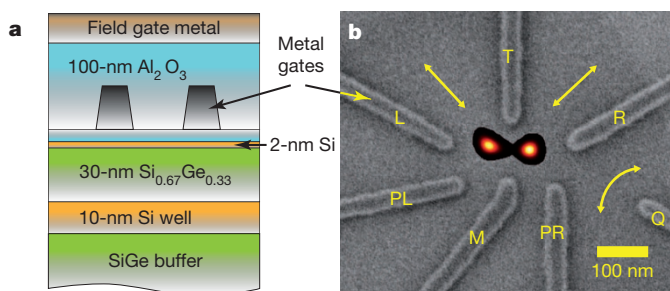


Figure 1 | Device design. **a**, Device cross-section showing undoped heterostructure, dielectric and gate stack. **b**, Scanning electron micrograph of actual device before dielectric isolation and field gate deposition. Electrostatic gates are labelled L (left), T, R (right), PL, M, PR and Q; gates L and R are used for fast pulsing. The straight arrows show current paths for transport experiments (Supplementary Information), whereas the curved arrow shows the path of current through the QPC. A numerical simulation of the electron density for the two-electron (1,1) state is superimposed on the micrograph.

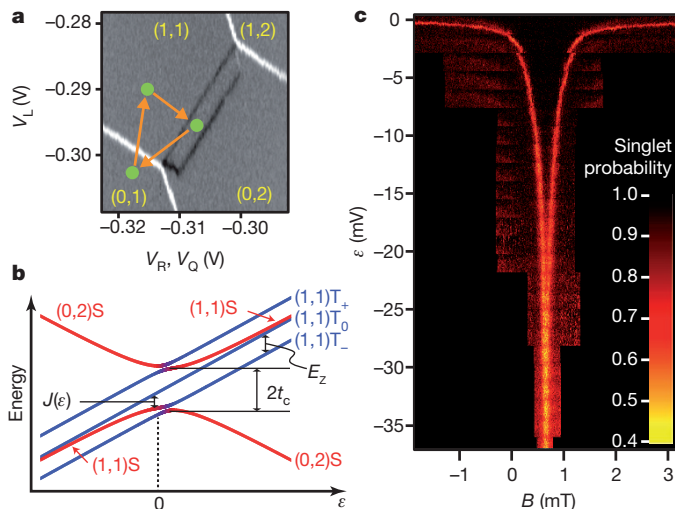


Figure 2 | Spin blockade in the double quantum dot. **a**, Subregion of the charge stability diagram, showing the differential transconductance (black and white lines) of the charge-sensing QPC as a function of gate voltages. The trapezoidal spin blockade signature is seen with cyclic pulsing through the sequence (0,1) → (1,1) → (0,2) (orange arrows). Being a differential measurement, the technique is sensitive only to changes in the average double-dot charge configuration, which is why only the edges of the trapezoidal blockade region are visible. The different colours indicate different responses of the QPC to electron movements on and between the dots. In particular, the current through the QPC decreases when electrons are added to either dot (white lines) but it increases when an electron transfers from the right dot to the left dot (black lines) (Supplementary Information). The voltage on gate Q (V_Q) was swept with that on gate R (V_R) to compensate for the capacitive coupling between gate R and the QPC and hence maintain constant sensitivity throughout the scan. **b**, Energy diagram of the (0,2)–(1,1) anticrossing, showing energies of the qubit states (1,1)S and (1,1) T_0 and the Zeeman split (1,1) T_{\pm} states as functions of detuning, ε . The exchange-energy splitting between qubit states, $J(\varepsilon)$, the Zeeman splitting between triplet states, E_Z , and the tunnel coupling, t_c , are shown. **c**, Spin funnel obtained by measuring the degeneracy of (1,1)S and (1,1) T_{\pm} as a function of ε and B . The width of the spin funnel implies a tunnel coupling, t_c , of approximately 3 μeV . The functional form of $J(\varepsilon)$ extracted from the funnel data is shown in Fig. 5.

The spin blockade is lifted by the presence of an excited state, observed when biasing deeper into the (0,2) charge region. The excited state opens an additional unblocked pathway and results in the trapezoidal blockade region seen in Fig. 2a. The trapezoid height indicates an excited state at an energy of approximately 140 μeV . Numerical modelling suggests that this state is a (0,2) triplet involving an excited valley state of the right-hand dot, but it could alternatively be an orbital triplet if the right-hand dot is highly asymmetric^{11,14}. In either case, the blockade region is sufficiently wide to distinguish the two qubit states (1,1)S and (1,1) T_0 , and all other excited states are high enough in energy to have no further role in coherent operation.

The coherent evolution of the singlet and triplet qubit states is governed by two interactions. First, the singlet–triplet energy splitting, which is primarily a result of hybridization of (1,1) and (0,2) singlets, acts as an effective exchange interaction with energy J between the two spins. Second, the dot-to-dot difference in the instantaneous hyperfine coupling to ^{29}Si nuclear spins (which comprise 4.7% of the lattice nuclei in isotopically natural silicon) acts as a singlet–triplet coupling energy, \mathcal{A}_{HF} . This coupling fluctuates from one experimental run to the next with a Gaussian distribution of standard deviation σ_{HF} . In a Bloch sphere picture with the singlet and triplet states at the poles, effective exchange causes a rotation about the z axis and the hyperfine energy introduces a random x component to this rotation axis. Experimentally, we have direct control over only J and are able to vary it by electrically pulsing the left- and right-hand gates to adjust the detuning, ε , between the dots (Fig. 2b). Because J and \mathcal{A}_{HF} provide independent rotation axes

and we only have direct control of J , exploration of the Bloch sphere requires us to achieve J values both much larger than and much smaller than σ_{HF} . For deep pulses into the (1,1) charge configuration, J is expected to be proportional to $t_c^2/|\varepsilon|$, where t_c is the interdot tunnel coupling²³. The tunnel coupling was kept small to access J values below the small σ_{HF} in silicon.

An estimate of the tunnel coupling is provided by measuring $J(\varepsilon)$ near $\varepsilon = 0$ in a ‘spin funnel’ experiment²⁴. An applied magnetic field, B , splits the (1,1) T_{\pm} states from (1,1) T_0 by the Zeeman energy, $E_Z = \pm g\mu_B B$, where μ_B is the Bohr magneton and g is the effective electron g factor in silicon. The energetic crossing of (1,1) T_- with (1,1)S occurs where $J(\varepsilon) = |E_Z|$ (Fig. 2b). At this crossing, hyperfine-induced mixing of (1,1)S and (1,1) T_- occurs, which is detected by the charge sensor as a spin blockade of the (1,1) T_- state. The detuning dependence of the energetic crossing point, corresponding to the form of $J(\varepsilon)$ as a function of B , resembles a funnel whose width can be used to estimate t_c (Fig. 2c). Using the funnel, we tuned our device until we obtained an acceptable t_c value of about 3 μeV .

Controlled rotations between superpositions of the singlet and triplet states may be achieved by modifying J . Such an experiment, following ref. 1, produces data analogous to Rabi oscillations. We start with the (0,2)S ground state and then slowly separate the electrons by biasing the dots deep into the (1,1) charge configuration (Fig. 3a, b). As a result of adiabatic passage (Supplementary Information and ref. 1), a low- J ground state is prepared that is a superposition of the (1,1)S and (1,1) T_0 states owing to the hyperfine field but, because J is non-zero, is not a hyperfine eigenstate. This superposition is rotated on the Bloch sphere by the non-adiabatically applied, larger- J exchange pulse. The rotation axis depends on both J and \mathcal{A}_{HF} (Fig. 3d). After the finite-duration exchange pulse, the gates are then pulsed back deep into (1,1) and adiabatically ramped into (0,2) for read-out. During this process, the low- J ground state is mapped back to the Pauli-unblocked hybridized singlet and the orthogonal low- J state is mapped to the Pauli-blocked triplet.

Figure 3c shows the resulting oscillation in the singlet probability, P_s , as a function of the exchange-pulse duration and detuning. At less negative detunings, corresponding to high values of J , the initial average visibility of the Rabi oscillations is 0.7 ± 0.1 . At more negative values of ε , corresponding to lower values of J , the initial visibility is reduced and hyperfine-induced damping is observed. At intermediate detunings, as many as 20 oscillations can be resolved. The average visibility, the damping at low J values and the phase modulation of the oscillations closely follow the behaviour expected when averaging over a Gaussian distribution of hyperfine differences \mathcal{A}_{HF} , as further described in Supplementary Information. Curve-fitting the data to this model allows us to extract $J(\varepsilon)$ over a wide bias range.

The practicality of implementing quantum computation using silicon-based double quantum dots depends on how long a separated (1,1)S state takes to dephase into an incoherent mixture of (1,1)S and (1,1) T_0 over multiple experimental runs. This timescale, T_2^* , directly impacts quantum control requirements, because it constrains either the speed or the complexity of high-fidelity gate operations. In III–V semiconductor quantum dots, T_2^* is reported to be a few to tens of nanoseconds^{1,2,5,25}. The measurement of T_2^* is accomplished by preparing a state orthogonal to the hyperfine rotation axis and then allowing it to evolve freely in many trials. In each trial, the hyperfine rotation frequency is different, such that on averaging over those trials a dephasing-induced decay is observed. In our double-dot system, we prepare the initial singlet state by biasing the device into the (0,2)S state and quickly (within ~ 20 ns) pulsing the gates to a large negative detuning deep in the (1,1) charge configuration (Fig. 4a, b). The pulsing is non-adiabatic with respect to the nuclear mixing time, so the separated electrons are initially in the (1,1)S state. The subsequent state precession is a function of both the instantaneous hyperfine gradient and the remaining exchange energy. As a result, an ensemble average both oscillates and dephases into a mixture of (1,1)S and

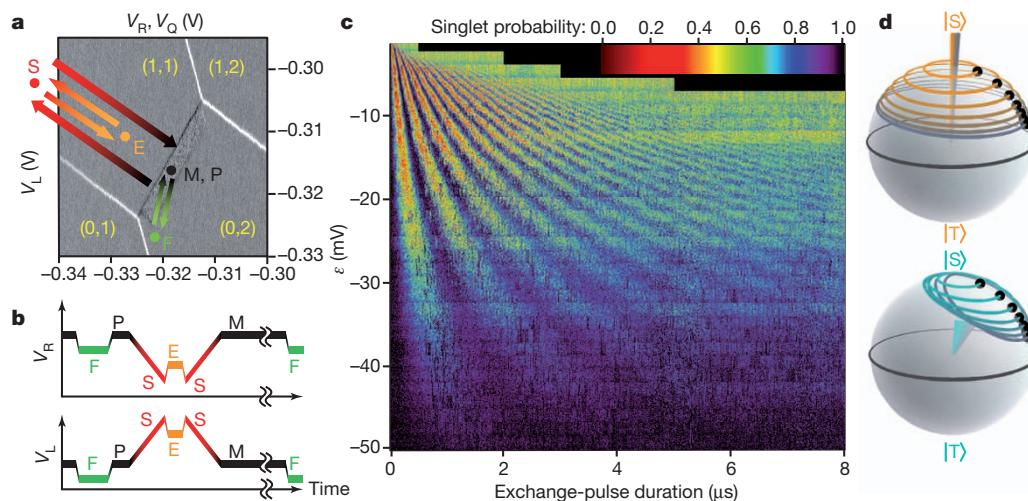


Figure 3 | Rabi oscillation pulse sequence and data. **a, b**, Essential elements of the pulse sequence used to obtain Rabi oscillations: V_L and V_R superimposed on the charge stability diagram (**a**); and represented as functions of time (**b**). The (0,2)S ground state is first prepared at point F with an exchange of an electron with the bath of the right-hand dot, if necessary. We then pulse to an intermediate point, P, before the subsequent adiabatic transition into the low- J ground state at point S, deep into (1,1). An exchange pulse and state rotation is then applied at E and followed by a return to S. The adiabatic transfer is then

reversed and the dots are biased to point M for measurement, which generally consists of $>90\%$ of the pulse cycle. **c**, Rabi oscillations of the singlet probability, P_s , as a function of ε and exchange-pulse duration. **d**, Bloch sphere representations of state evolution for $J > \sigma_{\text{HF}}$ (top) and $J < \sigma_{\text{HF}}$ (bottom). Several instances of initial hyperfine ground states are shown as black dots (all with $\Delta_{\text{HF}} > 0$, for clarity), with corresponding rotation axes and trajectories. The data in **c** correspond to the average probability of returning to the initial prepared low- J ground state.

(1,1) T_0 (refs 23, 26). The gates are then pulsed quickly back into the (0,2) charge configuration for measurement.

Figure 4c shows the measured ensemble-averaged singlet probability as a function of separation time for different detunings, corresponding to different values of residual exchange energy, J , present during the separation pulse. For moderate negative detunings ($J > \sigma_{\text{HF}}$), the singlet state rotates primarily around the z axis and the singlet probability remains close to 100% (Fig. 4d). For large negative detunings ($J < \sigma_{\text{HF}}$), the singlet state rotates around the x axis and dephases, bringing the singlet probability to approximately 50%. Intermediate detunings result in oscillation frequencies and asymptotic probabilities between these two extremes. Fitting the data in Fig. 4c with a consistent model^{23,26} for all traces provides estimates for the residual values of J and σ_{HF} (Supplementary Information). The extracted functional form of

$J(\varepsilon)$ is shown in Fig. 5 and is in excellent agreement with the values extracted from the Rabi oscillation periods where the two data sets overlap. The model yields an estimate for σ_{HF} of 2.6 ± 0.2 neV. A theoretical calculation of the expected σ_{HF} value in isotopically natural silicon, using real-space, hybrid Poisson–Schrödinger/full-configuration-interaction simulation methods, and using our best estimates of the microscopic device geometry and tuning configuration, yields a value for σ_{HF} of 1.9 neV (Supplementary Information and ref. 27), in reasonable agreement with the experimentally measured value. This value corresponds to a nuclei-induced dephasing time of $T_2^* = \sqrt{2}h/\sigma_{\text{HF}} = 360 \pm 30$ ns.

The reduced hyperfine coupling in silicon relative to other material systems will allow high-fidelity quantum control of future silicon-based qubits. Although the present device has only limited coherent

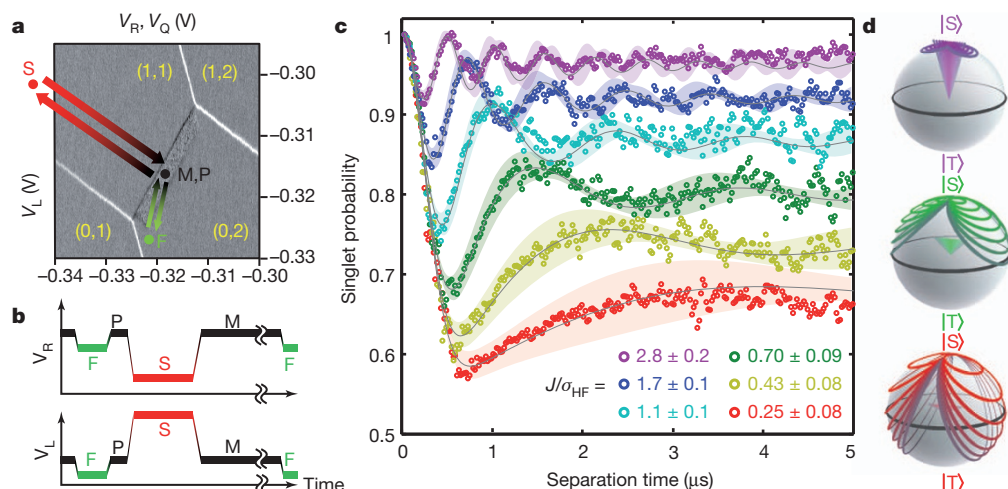


Figure 4 | T_2^* pulse sequence and data. **a, b**, Essential elements of T_2^* pulse sequence. Analogous with the Rabi oscillation pulse sequence (Fig. 3a, b), we initialize in the (0,2)S ground state at F and then pulse to intermediate point P. We then non-adiabatically pulse deeply into (1,1) to point S (this is the separation pulse) for a variable amount of time for singlet dephasing, and then return non-adiabatically to point M for measurement. **c**, Evolution of (1,1)S as indicated by P_s , as a function of separation time for several different separation-

pulse detunings (residual J). Coloured circles show measured data; the least-squares fit (black lines) and 1-s.d. confidence intervals (coloured bands) for a hyperfine-averaged model^{23,26} are superimposed. The values of J/σ_{HF} resulting from this fit are shown in the key. **d**, Bloch sphere representations of an ensemble of trajectories, with J/σ_{HF} values as indicated by colour in **c**. The ensemble of rotation axes is also shown in each case. The data in **c** correspond to the average projection of trajectories onto the z axis.

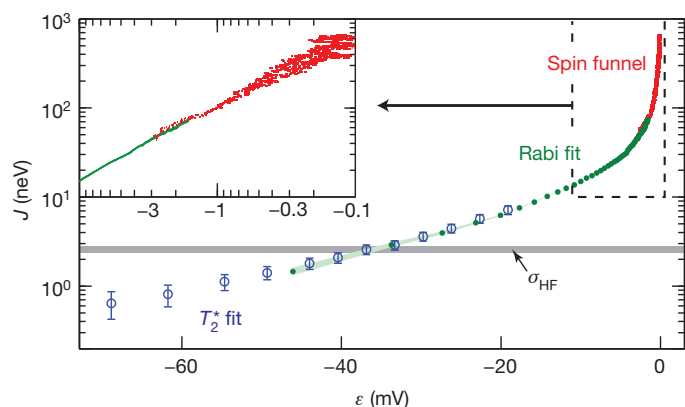


Figure 5 | Effective exchange energy versus detuning. $J(\epsilon)$ extracted from the spin funnel data (Fig. 2c), Rabi oscillation data (Fig. 3c) and T_2^* data (Fig. 4c). J ranges from 0.6 to 700 neV with excellent agreement where these data sets overlap (Supplementary Information). Error bars on the T_2^* data (blue) and the confidence interval for the Rabi data (green) are 1-s.d. fit-parameter uncertainties; spin funnel symbol sizes correspond to Gaussian-fit transition widths. The grey band denotes the estimated σ_{HF} value from the T_2^* data.

control capabilities owing to its reliance on the small and fluctuating hyperfine field for one axis of control, future devices will almost certainly not rely on hyperfine interactions. Other control methods, such as exchange-only control of three-dot systems²⁸, will allow complete coherent manipulation on a timescale much shorter than T_2^* . There are no fundamental problems with delivering exchange pulses on subnanosecond timescales¹, which will further allow pulse compensation and dynamical decoupling techniques for high-fidelity gate operations^{29,30}. These techniques can be used in future efforts to study and eliminate other decoherence sources not yet isolated in the experiments described here. Our results therefore indicate strong potential for the execution of the quantum error correction protocols that allow sustained quantum computation in silicon-based systems.

METHODS SUMMARY

The device is characterized in a dilution refrigerator with an estimated effective electron temperature of 150 mK. The QPC conductance changes when electrons are loaded, unloaded or transferred between the dots and is used to determine the charge state of the quantum dots. Fast voltage pulses are applied to the left- and right-hand gates using a Tektronix 5014 arbitrary wave generator with low-pass filtering at its output. Measurements are conducted with an external in-plane magnetic field of 30 mT, except for the spin funnel experiment, in which the field is swept.

The differential transconductance measurement technique used is implemented by superimposing a low-frequency voltage square wave (generally 600–900 Hz) on the left-hand gate and using standard lock-in amplification techniques with a 30-ms time constant and 60-ms delay between measurements. The low-frequency square wave is achieved by concatenating an appropriate number of the higher-frequency coherent manipulation pulse sequences to bring the lock-in measurement frequency down to near the noise floor of our measurement system. The added square wave is present only during the measurement phase of the pulse sequences. Apart from a background signal resulting from coupling between the low-frequency square wave and the QPC, the differential transconductance measurement technique is sensitive only to changes in the QPC conductance resulting from changes in the double-dot charge state configuration. As a result, we see only lines marking the outlines of the charge stability regions and of the trapezoidal triplet blockade region in (0,2), instead of the more commonly seen QPC conductance plateaux.

More details on experimental methods are available in Supplementary Information.

Received 24 June; accepted 1 November 2011.

- Petta, J. R. *et al.* Coherent manipulation of coupled electron spins in semiconductor quantum dots. *Science* **309**, 2180–2184 (2005).

- Koppens, F. H. L., Nowack, K. C. & Vandersypen, L. M. K. Spin echo of a single electron spin in a quantum dot. *Phys. Rev. Lett.* **100**, 236802 (2008).
- Reilly, D. J. *et al.* Suppressing spin qubit dephasing by nuclear state preparation. *Science* **321**, 817–821 (2008).
- Barthel, C., Medford, J., Marcus, C. M., Hanson, M. P. & Gossard, A. C. Interlaced dynamical decoupling and coherent operation of a singlet-triplet qubit. *Phys. Rev. Lett.* **105**, 266808 (2010).
- Bluhm, H. *et al.* Dephasing time of GaAs electron-spin qubits coupled to a nuclear bath exceeding 200 μ s. *Nature Phys.* **7**, 109–113 (2011).
- Simmons, S. *et al.* Entanglement in a solid-state spin ensemble. *Nature* **470**, 69–72 (2011).
- Tyryshkin, A. M. *et al.* Electron spin coherence exceeding seconds in high purity silicon. *Nature Mater.* (in the press); preprint at (<http://arxiv.org/abs/1105.3772>) (2011).
- Ladd, T. D. *et al.* Quantum computers. *Nature* **464**, 45–53 (2010).
- Kane, B. E. A silicon-based nuclear spin quantum computer. *Nature* **393**, 133–137 (1998).
- Eriksson, M. A. *et al.* Spin-based quantum dot quantum computing in silicon. *Quantum Inf. Process.* **3**, 133–146 (2004).
- Borselli, M. G. *et al.* Pauli spin blockade in undoped Si/SiGe two-electron double quantum dots. *Appl. Phys. Lett.* **99**, 063109 (2011).
- Goswami, S. *et al.* Controllable valley splitting in silicon quantum devices. *Nature Phys.* **3**, 41–45 (2007).
- Xiao, M., House, M. G. & Jiang, H. W. Parallel spin filling and energy spectroscopy in few-electron Si metal-on-semiconductor-based quantum dots. *Appl. Phys. Lett.* **97**, 032103 (2010).
- Borselli, M. G. *et al.* Measurement of valley splitting in high-symmetry Si/SiGe quantum dots. *Appl. Phys. Lett.* **98**, 123118 (2011).
- Lai, N. S. *et al.* Pauli spin blockade in a highly tunable silicon double quantum dot. *Sci. Rep.* **1**, 110 (2011).
- Hayes, R. R. *et al.* Lifetime measurements (T_1) of electron spins in Si/SiGe quantum dots. Preprint at (<http://arxiv.org/abs/0908.0173>) (2009).
- Xiao, M., House, M. G. & Jiang, H. W. Measurement of the spin relaxation time of single electrons in a silicon metal-oxide-semiconductor-based quantum dot. *Phys. Rev. Lett.* **104**, 096801 (2010).
- Morello, A. *et al.* Single-shot readout of an electron spin in silicon. *Nature* **467**, 687–691 (2010).
- Simmons, C. B. *et al.* Tunable spin loading and T_1 of a silicon spin qubit measured by single-shot readout. *Phys. Rev. Lett.* **106**, 156804 (2011).
- Johnson, A. C. *et al.* Triplet-singlet spin relaxation via nuclei in a double quantum dot. *Nature* **435**, 925–928 (2005).
- Liu, H. W. *et al.* Pauli-spin-blockade transport through a silicon double quantum dot. *Phys. Rev. B* **77**, 073310 (2008).
- Shaji, N. *et al.* Spin blockade and lifetime-enhanced transport in a few-electron Si/SiGe double quantum dot. *Nature Phys.* **4**, 540–544 (2008).
- Laird, E. A. *et al.* Effect of exchange interaction on spin dephasing in a double quantum dot. *Phys. Rev. Lett.* **97**, 056801 (2006).
- Petta, J. R. *et al.* Dynamic nuclear polarization with single electron spins. *Phys. Rev. Lett.* **100**, 067601 (2008).
- Press, D. *et al.* Ultrafast optical spin echo in a single quantum dot. *Nature Photon.* **4**, 367–370 (2010).
- Coish, W. A. & Loss, D. Singlet-triplet decoherence due to nuclear spins in a double quantum dot. *Phys. Rev. B* **72**, 125337 (2005).
- Assali, L. V. C. *et al.* Hyperfine interactions in silicon quantum dots. *Phys. Rev. B* **83**, 165301 (2011).
- DiVincenzo, D. P., Bacon, D., Kempe, J., Burkard, G. & Whaley, K. B. Universal quantum computation with the exchange interaction. *Nature* **408**, 339–342 (2000).
- Tomita, Y., Merrill, J. T. & Brown, K. R. Multi-qubit compensation sequences. *N. J. Phys.* **12**, 015002 (2010).
- West, J. R., Lidar, D. A., Fong, B. H. & Gyure, M. F. High fidelity quantum gates via dynamical decoupling. *Phys. Rev. Lett.* **105**, 230503 (2010).

Supplementary Information is linked to the online version of the paper at www.nature.com/nature.

Acknowledgements We thank C. M. Marcus for discussions, J. R. Petta for assistance with measurement techniques and B. H. Fong for assistance with hyperfine calculations. Sponsored by United States Department of Defense. The views and conclusions contained in this document are those of the authors and should not be interpreted as representing the official policies, either expressly or implied, of the United States Department of Defense or the US Government. Approved for public release, distribution unlimited.

Author Contributions B.M.M., M.G.B., C.A.W., K.S.H. and A.T.H. contributed to device measurement and testing. B.H., P.W.D., I.A.-R., A.E.S. and M.S. contributed to material growth and device fabrication. B.M.M., T.D.L., A.A.K., R.S.R. and M.F.G. contributed to modelling and data analysis. B.M.M., T.D.L., A.A.K. and M.F.G. prepared the manuscript.

Author Information Reprints and permissions information is available at www.nature.com/reprints. The authors declare no competing financial interests. Readers are welcome to comment on the online version of this article at www.nature.com/nature. Correspondence and requests for materials should be addressed to B.M.M. (bmmaune@hrl.com).